

# Polycrystalline anatase titanium dioxide microring resonators with negative thermo-optic coefficient

ORAD RESHEF,<sup>1</sup> KATIA SHTYRKOVA,<sup>2</sup> MICHAEL G. MOEBIUS,<sup>1</sup> SARAH GRIESSE-NASCIMENTO,<sup>1</sup> STEVEN SPECTOR,<sup>3</sup> CHRISTOPHER C. EVANS,<sup>1,4</sup> ERICH IPPEN,<sup>2</sup> AND ERIC MAZUR<sup>1,\*</sup>

<sup>1</sup>School of Engineering and Applied Sciences, Harvard University, 9 Oxford Street, Cambridge, Massachusetts 02138, USA

<sup>2</sup>Department of Electrical Engineering and Computer Science, Massachusetts Institute of Technology, 77 Massachusetts Avenue, Cambridge, Massachusetts 02139, USA

<sup>3</sup>Lincoln Laboratory, Massachusetts Institute of Technology, 244 Wood Street, Lexington, Massachusetts 02420, USA

<sup>4</sup>Kavli Institute at Cornell for Nanoscale Science, Cornell University, Ithaca, New York 14853, USA

\*Corresponding author: mazur@seas.harvard.edu

Received 13 July 2015; revised 3 September 2015; accepted 6 September 2015; posted 18 September 2015 (Doc. ID 245825); published 12 October 2015

We fabricate polycrystalline anatase TiO<sub>2</sub> microring resonators with loaded quality factors as high as 25,000 and average losses of 0.58 dB/mm in the telecommunications band. Additionally, we measure a negative thermo-optic coefficient  $dn/dT$  of  $-4.9 \pm 0.5 \times 10^{-5} \text{ K}^{-1}$ . The presented fabrication uses CMOS-compatible lithographic techniques that take advantage of substrate-independent, non-epitaxial growth. These properties make polycrystalline anatase a promising candidate for the implementation of athermal, vertically integrated, CMOS-compatible nanophotonic devices for nonlinear applications. © 2015 Optical Society of America

**OCIS codes:** (130.3120) Integrated optics devices; (130.3130) Integrated optics materials; (230.5750) Resonators; (160.6840) Thermo-optical materials.

<http://dx.doi.org/10.1364/JOSAB.32.002288>

## 1. INTRODUCTION

Titanium dioxide (TiO<sub>2</sub>) is a promising nanophotonic material due to its high transparency in the visible [1–8] and its applications for integrated nonlinear optics [9–12]. Its multiple phases (rutile, anatase, and brookite) each possess a large bandgap greater than 3 eV [13], yielding high transparency for wavelengths  $\lambda \geq 400 \text{ nm}$  spanning the visible and telecommunication bands. Unlike other high-index photonic platforms, such as silicon or chalcogenide glasses, TiO<sub>2</sub> photonic circuits can operate with virtually no two-photon absorption for  $\lambda \geq 800 \text{ nm}$  and without three-photon absorption over the entire telecom band [10]. TiO<sub>2</sub> has a linear index above  $n = 2.4$  in the optical regime and a nonlinear index approximately 30 times that of silica, making it favorable to transparent materials such as Al<sub>2</sub>O<sub>3</sub>, SiO<sub>2</sub>, SiN<sub>x</sub> or diamond for nonlinear applications. TiO<sub>2</sub> has the potential to achieve larger effective nonlinearities than these alternative materials [11]. These properties make TiO<sub>2</sub> an interesting platform for nonlinear optics research in the near-infrared.

Recently, TiO<sub>2</sub> has attracted attention for its use in athermal (i.e., temperature insensitive) photonic devices, particularly for applications that are wavelength sensitive [4,14–19]. Athermal

operation can be achieved using the material's negative thermo-optic coefficient (TOC,  $dn/dT$ , where  $n$  is the refractive index and  $T$  is the temperature) when paired with a positive TOC material. For example, ring resonators fabricated from materials with positive TOCs have been clad with amorphous TiO<sub>2</sub> in order to obtain an effective TOC near zero for over 30°C at 1.3 and 1.55  $\mu\text{m}$  [4,16,17,20]. Although this effect has also been achieved using polymers [21], which are widely known to possess negative TOCs [22], TiO<sub>2</sub> has the benefit of being CMOS compatible and can therefore be used in vertical integration schemes, drastically increasing device density on a chip [23].

In this paper, we demonstrate the first anatase TiO<sub>2</sub> microring resonators and use them to evaluate the quality of our fabrication process and to confirm the expected negative TOC of anatase. While the TOC of other phases of TiO<sub>2</sub> has been reported [17–19], the TOC of the anatase phase has not been studied in the telecommunications band. So far, anatase is unique in that it is the only phase of TiO<sub>2</sub> in which nonlinear processes such as spectral broadening [11] and third-harmonic generation [12] have been reported in a photonic integrated circuit. In contrast, these observations have remained elusive in rutile and amorphous TiO<sub>2</sub> due to their challenging fabrication

and photochromism, respectively [7,24,25]. Finally, polycrystalline anatase TiO<sub>2</sub> can be deposited at low temperatures (e.g., 600 K) on amorphous substrates, ensuring compatibility with a variety of CMOS processes.

## 2. THEORY

### A. Transmission Characteristics of a Microring Resonator

The spectral dependence of the transmission of a ring resonator with an input port and no add or through port has been thoroughly characterized and can be derived analytically using the scattering matrix approach [26–28],

$$T = \left| \frac{t - \alpha e^{i\phi}}{1 - \alpha t e^{i\phi}} \right|^2, \quad (1)$$

where  $t$  is the transmission (or self-coupling) coefficient corresponding to the fraction of the field that does not couple into the ring after a single pass,  $\alpha$  is the total relative field that is not lost in a round trip, and  $\phi$  is the round-trip phase shift.  $\phi$  varies as a function of wavelength  $\lambda$ , effective index  $n_{\text{eff}}$ , and propagation length  $L$ :

$$\phi = 2\pi \frac{n_{\text{eff}}}{\lambda} L. \quad (2)$$

The transmission curve has characteristic resonance peaks at the points where the numerator of Eq. (1) goes to zero. Additionally, significantly strong reflections at the facets create simultaneous counterpropagation within the ring that yields asymmetric resonances [29,30]. Using the scattering matrix approach [27], we derive the asymmetric transmission for this type of device to be

$$T = \left| \frac{(1 - \alpha t e^{i\phi})(t - \alpha e^{i\phi})}{\gamma e^{i\phi}(t - \alpha e^{i\phi})^2 - (1 - \alpha t e^{i\phi})^2} \right|^2, \quad (3)$$

where the additional coefficients  $\varphi$  and  $\gamma$  determine the shape and magnitude of the asymmetry. The variables  $\varphi$  and  $\gamma$  correspond, respectively, to the phase difference between the two counterpropagating waves and the losses resulting from both propagation through the waveguide and transmission through the facets at the ends. By fitting Eq. (3) to a particular resonance, we can extract  $\alpha$  and use it to compute a propagation loss  $\alpha_z$  for the waveguide that makes up the ring resonator. For a critically coupled resonator ( $\alpha = t$ ), the propagation loss can also be estimated using the group index  $n_g$  and the loaded  $Q$  to be [23]

$$\alpha_z = \frac{\pi n_g}{Q \lambda_0}. \quad (4)$$

These equations provide a method for accurately characterizing fabricated ring resonators, and extracting propagation losses.

### B. Effective Thermo-Optic Coefficients

Heating the sample induces a temperature-dependent refractive index change in the constituent materials, which can be characterized very precisely using a resonator. In a cavity structure such as a ring resonator, changing the temperature tunes the resonant wavelength  $\lambda_0$  by changing the index of the resonator material and via thermal expansion of the substrate. We quantify this change using [21,31]:

$$\frac{d\lambda_0}{dT} = \left( \frac{dn_{\text{eff}}}{dT} + n_{\text{eff}} \alpha_{\text{Si}} \right) \frac{\lambda_0}{n_g}. \quad (5)$$

Equation (5) includes a term for the thermal expansion coefficient of silicon ( $\alpha_{\text{Si}} = 2.59 \times 10^{-6} \text{ K}^{-1}$ ) [32]. Due to the geometry, the silicon substrate dominates the mechanical properties and thermal expansion of the sample. This new term represents the primary effect of thermal expansion on our device, which is to increase the diameter of the rings and shift the resonances toward longer wavelengths. Because the change in waveguide cross section due to thermal expansion is negligible, the group index does not change significantly to a first approximation.

We use the measured value of  $d\lambda_0/dT$  to estimate the change in index of the component materials. A waveguide that consists of a substrate, a core material, and an overcladding material has an effective index  $n_{\text{eff}}$  that we approximate by

$$n_{\text{eff}} \approx \Gamma_s n_s + \Gamma_c n_c + \Gamma_o n_o, \quad (6)$$

where  $\Gamma$  represents the power confinement factor within the individual materials and the subscripts  $s$ ,  $c$ , and  $o$  stand for substrate, core, and overcladding materials, respectively. This equation yields a very good first approximation for  $dn_{\text{eff}}/dT$  by differentiating [15]:

$$\frac{dn_{\text{eff}}}{dT} \approx \Gamma_s \frac{dn_s}{dT} + \Gamma_c \frac{dn_c}{dT} + \Gamma_o \frac{dn_o}{dT}. \quad (7)$$

For small changes in material index, we assume that the power confinement factors remain constant. Given measured TOCs of the cladding materials, we use Eq. (7) with Eq. (5) to estimate the thermo-optic coefficient of the core material.

## 3. EXPERIMENTAL

### A. Fabrication

We fabricate devices using methods described by Bradley *et al.* [1]. We structure waveguides from a 250-nm-thick polycrystalline anatase film that is deposited using RF magnetron sputtering at 600 K on an oxidized silicon substrate. The waveguides are defined by electron beam lithography and reactive ion etching, leaving our final desired structures on the silica substrate. The final fabricated chip is top-cladded with a low-index ( $n = 1.33$  at  $\lambda = 1550 \text{ nm}$ ) transparent polymer (CYTOP) to further reduce losses and protect the devices [Fig. 1(a)]. The ends of the chip are cleaved to prepare end facets.

The waveguides are designed to support a single mode throughout the wavelengths of operation (1525–1575 nm). The waveguides are trapezoidal in shape, with a width of 900 nm on top, 1035 nm at the base, and a sloped sidewall of approximately 75° due to the etch chemistry and substrate power [Fig. 1(a)]. This structure supports hybrid modes with <1% polarization mixing; therefore, we treat them as pure modes [Fig. 2(a)]. The ring resonators are coupled via a single 6.4-mm-long bus waveguide and have ring-waveguide coupling gaps of 250, 300, and 350 nm, and ring diameters of 200 and 300  $\mu\text{m}$  [Figs. 1(b) and 1(c)]. These dimensions are designed to ensure a free spectral range (FSR) larger than 1.2 nm (150 GHz) and to achieve near critical-coupling within the wavelengths of operation.

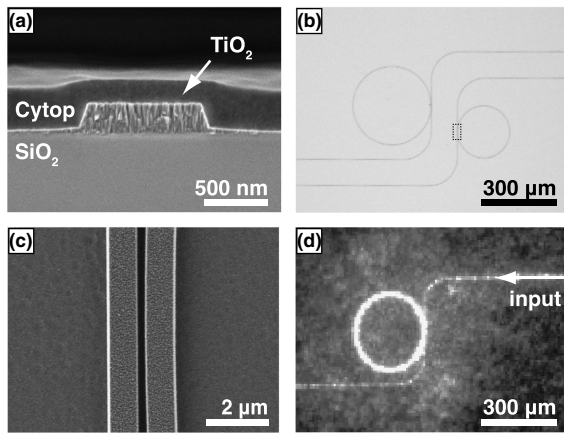


**Fig. 1.** (a) Cross section of the  $\text{TiO}_2$  waveguide, showing the embedded polycrystalline grains. The device is composed of a  $\text{TiO}_2$  waveguide on a thermal oxide substrate and cladded by a CYTOP polymer. The sidewalls are sloped at  $75^\circ$ . (b) Microscope image of a pair of anatase microring resonators with coupling bus waveguides. (c) Scanning electron microscope image of the coupling region indicated in (b), showing the polycrystalline grains on the surface and a 250-nm gap. (d) A 300- $\mu\text{m}$  diameter anatase microring operating near  $\lambda = 1550$  nm.

## B. Measurement Setup

We couple in and out of the waveguides using a pair of 0.85-NA objectives on three-axis stages. We launch 1525–1575 nm light using a tunable laser source with an input power of 4.1 mW and a resolution of 5 pm [Fig. 1(d)]. We select only transverse magnetic (TM)-polarized light (i.e., electric field polarized perpendicular to the plane of the device). We use a pellicle beam splitter before the devices and a pair of InGaAs photodiode detectors to measure the output power and the input power simultaneously to normalize the total transmission.

To measure the thermo-optic coefficient, the fabricated chip is placed on a conductive aluminum slab mounted on a heater. The light is coupled in and out of the waveguides using a tapered lensed fiber with a 2.5- $\mu\text{m}$  spot size on the input and a microscope objective on the output facet. The objective directs the output light onto either an IR camera used for alignment or an InGaAs detector used for taking data. A polarizer located between the objective and the detector allows us to determine the input and output polarizations of light. We excite the TM mode and measure the spectrum of several high- $Q$  resonances at multiple temperatures from  $24^\circ\text{C}$  to  $37^\circ\text{C}$ .

## 4. RESULTS

We couple into and out of the  $\text{TiO}_2$  bus waveguides, yielding total insertion losses off-resonance as low as 10 dB for the propagation of the TM-polarized mode. Figure 2(b) shows a typical transmission spectrum for a ring with a diameter of 300  $\mu\text{m}$  and coupling gap of 300 nm. It shows distinct, equally spaced resonances that deepen for longer wavelengths with extinction ratios ranging from 2.3 to 10.5 dB, achieving near-critical coupling at the longest wavelengths. Some of the resonances show an asymmetry. This asymmetry is independent of wavelength sweep direction or input power. The measured

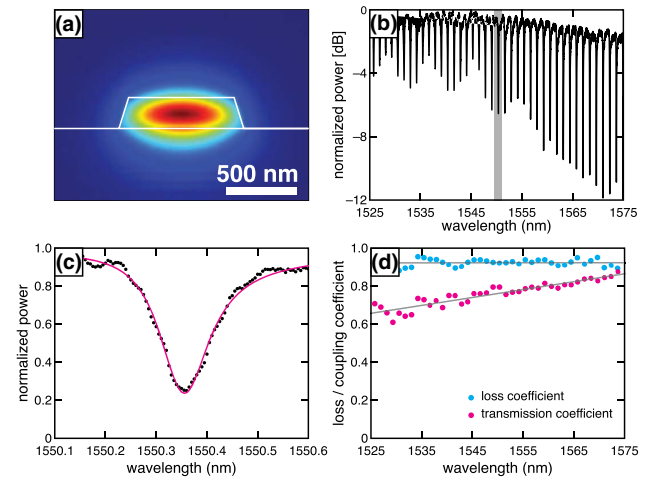


**Fig. 2.** (a) Energy density for TM-polarized guided mode at  $\lambda = 1550$  nm. (b) Transmission spectrum of a 300- $\mu\text{m}$  diameter, 300-nm gap anatase ring resonator. The resonances get deeper for longer wavelengths, with a loaded quality factor as high as  $2.0 \times 10^4$  at  $\lambda = 1571$  nm. (c) A fit to an asymmetric resonance at  $\lambda = 1550$  nm indicated in gray in (b). This fit yields a transmission coefficient  $t$  of 0.798 and a loss coefficient  $\alpha$  of 0.911, corresponding to a propagation loss of 0.77 dB/mm. (d) Extracted transmission coefficients  $t$  and loss coefficients  $\alpha$  for each resonance. The linear fits are a guide to the eye, showing that  $\alpha$  remains constant, indicating that the propagation loss does not change significantly over this wavelength range.

FSR for the 200- and 300- $\mu\text{m}$  diameter rings is 236 and 157 GHz, respectively. We compare these values to theoretical values computed using  $\text{FSR} = c/(n_g L)$  using a simulated group index of  $n_g = 2.03$ . We calculate the FSR of the 200- and 300- $\mu\text{m}$  diameter rings to be 235 and 157 GHz, respectively (Table 1).

For the 200- $\mu\text{m}$  diameter rings, we obtain  $Q$ -factors of  $10^3$  with a maximum observed loaded  $Q$ -factor of  $5.5 \times 10^3$  with a gap of 250 nm. For the 300- $\mu\text{m}$  diameter rings, we obtain  $Q$ -factors of  $10^4$  with a maximum observed loaded  $Q$ -factor of  $2.5 \times 10^4$  with a gap of 250 nm.

We fit the transmission spectra for asymmetric resonances from  $\lambda = 1525$  to 1575 nm to Eq. (3) [Fig. 2(c)] and extract the transmission coefficient  $t$  and the loss coefficient  $\alpha$  [Fig. 2(d)]. We note that the loss coefficients are smaller for

**Table 1. Free Spectral Range (FSR) and Propagation Losses near  $\lambda = 1550$  nm for Different Devices and Coupling Gaps<sup>a</sup>**

Ring Diameter [ $\mu\text{m}$ ]	Gap Size [nm]	Theoretical FSR [GHz]	Measured FSR [GHz]	Propagation Loss $\alpha_z$ [dB/mm]
200	250	235	235	1.90
200	300	235	235	2.58
200	350	235	238	3.10
300	250	157	156	0.40
300	300	157	157	0.69
300	350	157	158	0.72

<sup>a</sup>The propagation losses are calculated directly from  $\alpha$ .



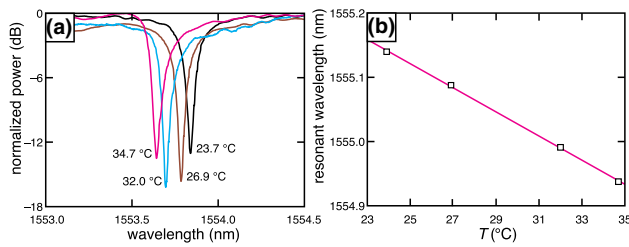


**Fig. 3.** (a) Raising the temperature blueshifts the resonance, corresponding to a negative TOC. (b) Fitting to the positions of the resonance peaks as a function of temperature yields a rate of  $d\lambda_0/dT = -19$  pm/K, corresponding to a  $dn_{\text{TiO}_2}/dT$  of  $-4.9 \pm 0.5 \times 10^{-5} \text{ K}^{-1}$ . The height of the box symbol represents the error in the fit to the curves in (a).

the larger ring diameter. The transmission coefficient is larger for the larger ring diameter as well. We calculate the corresponding power propagation losses for the fundamental TM-polarized mode directly from  $\alpha$  using  $\alpha^2 = e^{-\alpha_c 2\pi R}$ . We average the propagation losses extracted from  $\lambda = 1545$  to  $1555$  nm and tabulate them in Table 1. Taking the geometric mean of the values in Table 1 yields an average propagation loss of 2.48 dB/mm for the 200- $\mu\text{m}$  rings, with a lower average loss of 0.58 dB/mm for the 300- $\mu\text{m}$  rings. The lowest propagation loss obtained is 0.40 dB/mm found for a 300- $\mu\text{m}$  ring.

We vary the temperature and we probe a 300- $\mu\text{m}$  diameter ring with a gap of 300 nm around  $\lambda = 1555$  nm. We observe that the location, symmetry, and depth of one of the sharper resonances in the spectrum change as a function of temperature [Fig. 3(a)]. At higher temperatures, the location of the resonance blueshifts at a rate of  $d\lambda_0/dT = -19$  pm/K [Fig. 3(b)], corresponding to a change in effective index of  $dn_{\text{eff}}/dT = -2.86 \times 10^{-5} \text{ K}^{-1}$ .

The TOC of the anatase thin film is difficult to measure directly as it is deposited on a thick oxide substrate. The thickness of the substrate creates many fringes in the ellipsometric profile, making it difficult to obtain an accurate fit for the optical constants. To determine the contribution of each layer to the measured  $dn_{\text{eff}}/dT$  of the device, we simulate the power confinement factors for the three regions using a commercial finite-element eigenmode solver, setting both the substrate and overcladding thickness to 3  $\mu\text{m}$  (Table 2). Changing the cladding index from 1.33 to 1.45 has a minimal effect on the core confinement of the mode. The errors in the power factors are estimated using the errors in the measurement for the material parameters, the measurement error for the

waveguide geometry (determined using scanning electron microscopy and atomic force microscopy), and the finite mesh used in the solver. We measure  $dn/dT$  for  $\text{SiO}_2$  and CYTOP thin films directly using temperature-controlled ellipsometry (Table 2). Inserting these values into Eq. (7) yields a TOC for  $\text{TiO}_2$  of  $dn_{\text{TiO}_2}/dT = -4.9 \pm 0.5 \times 10^{-5} \text{ K}^{-1}$ .

## 5. DISCUSSION

To quantify the accuracy of our fabrication and measurement process, we compare our measured FSRs to simulation results. The measured FSRs increase as the ring circumferences decrease and agree with theoretical values within 0.5%. Additionally, these results, as well as the lack of additional resonances, confirm that we are exciting only TM-polarized modes within the resonators. TE-polarized modes yield drastically smaller FSRs of 127 and 190 GHz for the 300- and 200- $\mu\text{m}$  diameter rings, respectively, because their group index is comparatively larger (e.g.,  $n_g = 2.51$  for TE versus  $n_g = 2.03$  for TM) than for a TM-polarized mode. This agreement affirms the robustness of our simulations, material parameters, and tight fabrication tolerance.

We can verify the fits to Eq. (3) by reviewing the extracted coefficients in Fig. 2(d). First, we observe little variation in  $\alpha$ , as expected from Rayleigh scattering within this wavelength range. Conversely,  $t$  changes with wavelength. A constant coefficient is observed in all of the measured devices, and it is how we unambiguously distinguish  $\alpha$  from  $t$  [28].

These fits also yield coefficients from which we can estimate the propagation loss within the rings. The mean propagation loss for the larger rings is 0.58 dB/mm at  $\lambda = 1550$  nm. This value is comparable to the propagation losses that have been previously cited for polycrystalline anatase (0.4–0.8 dB/mm) [1,11]. Additionally, it is calculated based on the more accurate resonator-based method than the top-down imaging-based loss extraction method used previously. A loss of 0.58 dB/mm compares favorably to early results using polycrystalline silicon, another material which is expected to exhibit similar scattering losses and has reported propagation losses as low as 0.9 dB/mm for films of a similar thickness [33]. The grains in these polycrystalline films, which contribute to the surface roughness and thus the scattering loss [1,23], are of the order of 50 nm, less than  $\lambda/30$ . Prism coupling measurements for TM-polarized light at  $\lambda = 1550$  nm in the thin films fabricated for this work yield losses of 0.33 dB/mm. Our lowest device losses (0.40 dB/mm) are similar to these planar-waveguide measurements, indicating that the film itself is a limiting source of loss in our devices.

The propagation losses take into account both bending losses and scattering losses due to the polycrystalline structure and fabrication imperfections. The measured propagation loss in the rings increases by a factor of 4 when decreasing the bend radius from 300 to 200  $\mu\text{m}$  (0.58 versus 2.48 dB/mm). A larger propagation loss implies that bending losses have become significant. However, finite element simulations predict no large bending loss associated with a 100- $\mu\text{m}$  bend radius. Alternatively, since a guided mode is pushed toward the outer wall in a ring with sharper bends, larger losses imply that the sidewalls of the waveguide have an increased roughness due to

**Table 2. Simulated Power Confinement Factors for a  $900 \times 250$  nm  $\text{TiO}_2$  Waveguide<sup>a</sup>**

Region	Material	Confinement	TOC
		factor $\Gamma$	$dn/dT$ [ $\text{K}^{-1}$ ]
Cladding	CYTOP	$24.2 \pm 0.4\%$	$-9.7 \pm 0.2 \times 10^{-5}$
Core	$\text{TiO}_2$	$29.4 \pm 1.6\%$	$-4.9 \pm 0.5 \times 10^{-5}$
Substrate	$\text{SiO}_2$	$46.4 \pm 1.4\%$	$2.0 \pm 0.2 \times 10^{-5}$

<sup>a</sup>The TOC for  $\text{SiO}_2$  and CYTOP were measured on thin films using temperature-controlled ellipsometry. The TOC for  $\text{TiO}_2$  was calculated using Eq. (7).

the fabrication process. Thus, we conclude that fabrication imperfections are the dominant contribution to the propagation losses in this context. This also explains why devices performed better under TM excitation when compared to TE excitation: the TE mode suffers from higher losses due to stronger localization of the fields near the rough fabrication boundaries. Our fabrication methods can be further optimized to minimize propagation losses by adopting a more optimal etch chemistry [34] or by using resist reflow techniques [35].

Minimum total insertion losses of 10 dB with a minimum waveguide propagation loss of 0.40 dB/mm are realistic values for our devices. Given a 6.4-mm-long waveguide, we calculate a waveguide loss of 2.6 dB giving an insertion loss of 3.7 dB/facet. Finite element simulations yield a power overlap of 66.0% between the fundamental TM mode and a focused Gaussian beam spot using a numerical aperture of 0.85. This accounts for 1.8 dB of the insertion loss per facet, with the remaining 1.9 dB/facet arising due to scattering created during facet cleavage. The insertion loss could be lowered by mechanically polishing the waveguide facets.

Using the extracted losses above and Eq. (4), we estimate that the largest intrinsic quality factor  $Q_0$  for these rings is 89,000, corresponding to a theoretical maximum loaded  $Q$  of 44,500. However, the maximum observed loaded  $Q$  of 25,000 did reach this limit. We attribute this discrepancy to the fact that the resonators are operating in the overcoupled regime, which is confirmed by the fact that  $t$  is less than  $\alpha$  [Fig. 2(d)], as more light is lost to coupling than to propagation around the ring. The estimated  $Q_0$  still compares favorably to early results using polycrystalline silicon of 40,000 [23]. However, it remains an order of magnitude smaller than the highest reported  $Q$ -factors achieved in sol-gel-based amorphous  $\text{TiO}_2$  whispering gallery microcavities [6] and lifted-off amorphous  $\text{TiO}_2$  ring resonators [12].  $Q$ -factors of the order of  $10^4$  are large enough to observe some nonlinear processes, such as low-threshold harmonic generation, but improvements are necessary to demonstrate on-chip frequency combs or nonlinear interferometers, which typically require loaded quality factors greater than  $10^5$  [36,37].

The blueshifting of the resonance as a function of temperature depicted in Fig. 3 is consistent with a negative TOC, as has been reported previously for  $\text{TiO}_2$ . This shift cannot be attributed only to expansion because that would contribute solely to a redshift, displacing resonances toward longer wavelengths. We attribute the change in the depth of the resonances to a changing asymmetric phase term  $\varphi$ , corresponding to the round-trip phase in the bus waveguide. This term also changes as a function of effective index. Because we normalize the measured intensity to its maximum value, different asymmetries appear to produce different extinction values.

Our measured value of  $dn_{\text{TiO}_2}/dT = -4.9 \pm 0.5 \times 10^{-5} \text{ K}^{-1}$  is within an order of magnitude of prior literature values for the TOC of amorphous  $\text{TiO}_2$  ( $-1$  to  $-2 \times 10^{-4} \text{ K}^{-1}$ ) [6,17]. A more extensive study that varies the waveguides geometry and that probes a larger temperature range would be beneficial to further understand and optimize athermal anastase devices. This TOC enables athermal device designs that consist solely of  $\text{TiO}_2$  waveguides on a substrate, without the

need for a negative TOC cladding. A standard oxide cladding, such as  $\text{SiO}_2$ , can provide the balancing positive TOC. Using a finite element eigenmode solver and the TOC values reported above, we predict athermal operation dimensions for a  $\text{TiO}_2$  ring resonator cladded in  $\text{SiO}_2$  on a silicon substrate at  $\lambda = 1550 \text{ nm}$ . For TE polarization, the waveguide cross-sectional dimensions are 390 nm wide  $\times$  250 nm thick, while for TM polarization, the dimensions are 479 nm wide  $\times$  300 nm thick. These designs can form the basis for vertically integrated athermal photonic devices relying on a robust oxide material platform with high core-cladding index contrast.

In conclusion, we have fabricated and characterized high- $Q$  polycrystalline anatase  $\text{TiO}_2$  microring resonators. The material platform and fabrication techniques are scalable, CMOS compatible, do not require specialized substrates, and support vertically integrated photonic devices. Using these methods, we have obtained intrinsic  $Q$ -factors of up to 89,000, corresponding to losses as low as 0.40 dB/mm at  $\lambda = 1550 \text{ nm}$ . We report the first measurement of a negative TOC in anatase  $\text{TiO}_2$  at telecommunication wavelengths, which can be used in conjunction with CMOS-compatible positive TOC materials to fabricate vertically integrated athermal optical devices. Given these properties, anatase  $\text{TiO}_2$  is well-positioned to become an important material for wavelength-insensitive, device-dense integrated nanophotonics.

**Funding.** Air Force Office of Scientific Research (AFOSR) (FA8721-05-C-0002, FA9550-12-1-0499); Division of Electrical, Communications and Cyber Systems (ECCS) (1201976); Division of Physics (PHY) (1415236); Harvard Graduate Prize Fellowship; Harvard Quantum Optics Center; Kavli Institute at Cornell for Nanoscale Science Postdoctoral Fellowship; National Defense Science and Engineering Graduate Fellowship (32 CFR 168a); National Science Foundation (NSF) (DGE1144152) Graduate Research Fellowship Program; Natural Sciences and Engineering Research Council of Canada (NSERC).

**Acknowledgment.** Several people contributed to the work described in this paper. O. R. and K. S. conceived of the basic idea for this work. O. R. did the initial fabrication. O. R., K. S., and M. G. M. designed and carried out the experiments in the first section, and analyzed the results. C. C. E. aided in the analysis and interpretation. S. G.-N. and S. S. carried out the experiments pertaining to TOC and O. R., M. G. M., and S. G.-N. analyzed the results. The authors acknowledge the help of Philip Muñoz with statistics, Qimin Quan for providing materials, the help of Vladimir Liberman with the ellipsometry measurements, and the help of Sara Mouser with the TOC experiments. E. M. and E. I. supervised the research and the development of the manuscript. O. R. wrote the first draft of the manuscript; all authors subsequently took part in the revision process and approved the final copy of the manuscript. Benjamin Franta, Alexander W. Raymond, Yang Li, and Mei Yin provided feedback on the manuscript throughout its development. The authors acknowledge the use of facilities in the Center for Nanoscale Systems, which is supported by the National Science Foundation's National Nanotechnology

Infrastructure Network. Opinions, interpretations, conclusions, and recommendations are those of the authors and are not necessarily endorsed by the United States government.

## REFERENCES

- J. D. B. Bradley, C. C. Evans, J. T. Choy, O. Reshef, P. B. Deotare, F. Parsy, K. C. Phillips, M. Lončar, and E. Mazur, "Submicrometer-wide amorphous and polycrystalline anatase TiO<sub>2</sub> waveguides for micro-photonic devices," *Opt. Express* **20**, 23821–23831 (2012).
- M. Hayrinen, M. Roussey, V. Gandhi, P. Stenberg, A. Saynatjoki, L. Karvonen, M. Kuittinen, and S. Honkanen, "Low-loss titanium dioxide strip waveguides fabricated by atomic layer deposition," *J. Lightwave Technol.* **32**, 208–212 (2014).
- M. Furuhashi, M. Fujiwara, T. Ohshiro, K. Matsubara, M. Tsutsui, M. Taniguchi, S. Takeuchi, and T. Kawai, "Embedded TiO<sub>2</sub> waveguides for sensing nanofluorophores in a microfluidic channel," *Appl. Phys. Lett.* **101**, 153115 (2012).
- F. Qiu, A. M. Spring, F. Yu, I. Aoki, A. Otomo, and S. Yokoyama, "Thin TiO<sub>2</sub> core and electro-optic polymer cladding waveguide modulators," *Appl. Phys. Lett.* **102**, 233504 (2013).
- J. T. Choy, J. D. B. Bradley, P. B. Deotare, I. B. Burgess, C. C. Evans, E. Mazur, and M. Lončar, "Integrated TiO<sub>2</sub> resonators for visible photonics," *Opt. Lett.* **37**, 539–541 (2012).
- J. Park, S. K. Ozdemir, F. Monifi, T. Chadha, S. H. Huang, P. Biswas, and L. Yang, "Titanium dioxide whispering gallery microcavities," *Adv. Opt. Mater.* **2**, 711–717 (2014).
- Z.-F. Bi, L. Wang, X.-H. Liu, S.-M. Zhang, M.-M. Dong, Q.-Z. Zhao, X.-L. Wu, and K.-M. Wang, "Optical waveguides in TiO<sub>2</sub> formed by He ion implantation," *Opt. Express* **20**, 6712–6719 (2012).
- C. C. Evans, C. Liu, and J. Suntivich, "Low-loss titanium dioxide waveguides and resonators using a dielectric lift-off fabrication process," *Opt. Express* **23**, 11160–11169 (2015).
- A. Borne, P. Segonds, B. Boulanger, C. Félix, and J. Debray, "Refractive indices, phase-matching directions and third order nonlinear coefficients of rutile TiO<sub>2</sub> from third harmonic generation," *Opt. Mater. Express* **2**, 1797–1802 (2012).
- C. C. Evans, J. D. B. Bradley, E. A. Martí-Panameño, and E. Mazur, "Mixed two- and three-photon absorption in bulk rutile (TiO<sub>2</sub>) around 800 nm," *Opt. Express* **20**, 3118–3128 (2012).
- C. C. Evans, K. Shtyrkova, J. D. B. Bradley, O. Reshef, E. Ippen, and E. Mazur, "Spectral broadening in anatase titanium dioxide waveguides at telecommunication and near-visible wavelengths," *Opt. Express* **21**, 18582–18591 (2013).
- C. C. Evans, K. Shtyrkova, O. Reshef, M. Moebius, J. D. B. Bradley, S. Griesse-Nascimento, E. Ippen, and E. Mazur, "Multimode phase-matched third-harmonic generation in sub-micrometer-wide anatase TiO<sub>2</sub> waveguides," *Opt. Express* **23**, 7832–7841 (2015).
- M. Landmann, E. Rauls, and W. G. Schmidt, "The electronic structure and optical response of rutile, anatase and brookite TiO<sub>2</sub>," *J. Phys.* **24**, 195503 (2012).
- J. Bovington, R. Wu, K.-T. Cheng, and J. E. Bowers, "Thermal stress implications in athermal TiO<sub>2</sub> waveguides on a silicon substrate," *Opt. Express* **22**, 661–666 (2014).
- S. S. Djordjevic, K. Shang, B. Guan, S. T. S. Cheung, L. Liao, J. Basak, H.-F. Liu, and S. J. B. Yoo, "CMOS-compatible, athermal silicon ring modulators clad with titanium dioxide," *Opt. Express* **21**, 13958–13968 (2013).
- S. Feng, K. Shang, J. T. Bovington, R. Wu, K.-T. Cheng, J. E. Bowers, and S. J. B. Yoo, "Athermal characteristics of TiO<sub>2</sub>-clad silicon waveguides at 1.3 μm," in *IEEE Photonics Conference*, San Diego, California, 2014, pp. 116–117.
- B. Guha, J. Cardenas, and M. Lipson, "Athermal silicon microring resonators with titanium oxide cladding," *Opt. Express* **21**, 26557–26563 (2013).
- F. Zhang, R.-J. Zhang, D.-X. Zhang, Z.-Y. Wang, J.-P. Xu, Y.-X. Zheng, L.-Y. Chen, R.-Z. Huang, Y. Sun, X. Chen, X.-J. Meng, and N. Dai, "Temperature-dependent optical properties of titanium oxide thin films studied by spectroscopic ellipsometry," *Appl. Phys. Express* **6**, 121101 (2013).
- S. Wiechmann and J. Müller, "Thermo-optic properties of TiO<sub>2</sub>, Ta<sub>2</sub>O<sub>5</sub> and Al<sub>2</sub>O<sub>3</sub> thin films for integrated optics on silicon," *Thin Solid Films* **517**, 6847–6849 (2009).
- F. Qiu, A. M. Spring, and S. Yokoyama, "An athermal and high-Q hybrid TiO<sub>2</sub>-Si<sub>3</sub>N<sub>4</sub> ring resonator via an etching-free fabrication technique," *ACS Photonics* **2**, 405–409 (2015).
- P. Alipour, E. S. Hosseini, A. A. Eftekhari, B. Momeni, and A. Adibi, "Athermal performance in high-Q polymer-clad silicon microdisk resonators," *Opt. Lett.* **35**, 3462–3464 (2010).
- Z. Zhang, P. Zhao, P. Lin, and F. Sun, "Thermo-optic coefficients of polymers for optical waveguide applications," *Polymer* **47**, 4893–4896 (2006).
- K. Preston, B. Schmidt, and M. Lipson, "Polysilicon photonic resonators for large-scale 3D integration of optical networks," *Opt. Express* **15**, 17283–17290 (2007).
- R. J. Colton, A. M. Guzman, and J. W. Rabalais, "Photochromism and electrochromism in amorphous transition metal oxide films," *Acc. Chem. Res.* **11**, 170–176 (1978).
- Y. Ohko, T. Tatsuma, T. Fujii, K. Naoi, C. Niwa, Y. Kubota, and A. Fujishima, "Multicolour photochromism of TiO<sub>2</sub> films loaded with silver nanoparticles," *Nat. Mater.* **2**, 29–31 (2003).
- A. Yariv, "Universal relations for coupling of optical power between microresonators and dielectric waveguides," *Electron. Lett.* **36**, 321–322 (2000).
- J. E. Heebner, V. Wong, A. Schweinsberg, R. W. Boyd, and D. J. Jackson, "Optical transmission characteristics of fiber ring resonators," *IEEE J. Quantum Electron.* **40**, 726–730 (2004).
- W. R. McKinnon, D. X. Xu, C. Storey, E. Post, A. Densmore, A. Delâge, P. Waldron, J. H. Schmid, and S. Janz, "Extracting coupling and loss coefficients from a ring resonator," *Opt. Express* **17**, 18971–18982 (2009).
- S. Fan, "Sharp asymmetric line shapes in side-coupled waveguide-cavity systems," *Appl. Phys. Lett.* **80**, 908–910 (2002).
- T. Hu, P. Yu, C. Qiu, H. Qiu, F. Wang, M. Yang, X. Jiang, H. Yu, and J. Yang, "Tunable Fano resonances based on two-beam interference in microring resonator," *Appl. Phys. Lett.* **102**, 011112 (2013).
- F. Qiu, A. M. Spring, F. Yu, and S. Yokoyama, "Complementary metal-oxide-semiconductor compatible athermal silicon nitride/titanium dioxide hybrid micro-ring resonators," *Appl. Phys. Lett.* **102**, 051106 (2013).
- Y. Okada and Y. Tokumaru, "Precise determination of lattice parameter and thermal expansion coefficient of silicon between 300 and 1500 K," *J. Appl. Phys.* **56**, 314–320 (1984).
- L. Liao, D. R. Lim, A. M. Agarwal, X. Duan, K. K. Lee, and L. C. Kimerling, "Optical transmission losses in polycrystalline silicon strip waveguides: effects of waveguide dimensions, thermal treatment, hydrogen passivation, and wavelength," *J. Electron. Mater.* **29**, 1380–1386 (2000).
- K. T. Vu and S. J. Madden, "Reactive ion etching of tellurite and chalcogenide waveguides using hydrogen, methane, and argon," *J. Vac. Sci. Technol. A* **29**, 011023 (2011).
- R. Shankar, I. Bulu, and M. Lončar, "Integrated high-quality factor silicon-on-sapphire ring resonators for the mid-infrared," *Appl. Phys. Lett.* **102**, 051108 (2013).
- B. J. M. Hausmann, I. Bulu, V. Venkataraman, P. Deotare, and M. Lončar, "Diamond nonlinear photonics," *Nat. Photonics* **8**, 369–374 (2014).
- J. S. Levy, M. A. Foster, A. L. Gaeta, and M. Lipson, "Harmonic generation in silicon nitride ring resonators," *Opt. Express* **19**, 11415–11421 (2011).